https://doi.org/10.5194/egusphere-2026-1006
Preprint. Discussion started: 4 March 2026

Beyond Runoff Coefficient: Revealing Global Patterns of Process Connectivity in Runoff Generation through Intensity Integration

Hanxu Liang[1], Dedi Liu[1] *, Jiayu Zhang[1], Feng Yue[1], Yuling Zhang[1]

[1] State Key Laboratory of Water Resources Engineering and Management, Wuhan University, Wuhan, China

Correspondence to: Dedi Liu (dediliu@whu.edu.cn)

Abstract. Climate change and human activities have profoundly altered the connectivity of runoff generation (i.e., the transformation process from precipitation to runoff). It is critical to understand this connectivity for climate change adaptation and water-related risk management. However, the runoff coefficient (*RC*), as the most common connectivity indicator, only describes the ratio of precipitation transformed into runoff, failing to characterize the rate of the transformation. Here we develop a novel framework to assess process connectivity in runoff generation through intensity integration. The *RC* and runoff intensity (*RI*) are adopted to represent the transformation ratio and rate from precipitation to runoff, respectively, and a composite metric runoff efficiency (*RE*), calculated as the product of *RC* and *RI*, is proposed to capture both dimensions. Applying this framework to 6,603 catchments globally over 1950–2020, we quantify the spatial patterns of process connectivity, diagnose their influencing factors, and examine their long-term trends and event-scale responses to precipitation intensity. According to their multi-year average values, we find a relatively high *RC* and *RI* in wet and dry areas, respectively. Interpretable machine learning further reveals that climatic attributes primarily control the process connectivity globally. The results of long-term trends show that the hotspots of increasing process connectivity are South America and central North America, which are typically associated with a higher flood risk. Event-scale results indicate a high sensitivity of precipitation intensity on *RE* in dry climate zones. These findings not only enhance our understanding of runoff generation processes under the changing environment, but also offer valuable insights into adaptive water resources management.

1 Introduction

The global hydrological cycle is an integrated system of interconnected components, including evapotranspiration, atmospheric water vapour, precipitation, snowmelt, runoff, etc. (Yang et al., 2021; Oki and Kanae, 2006). Hydrological connectivity, defined as the water transfer within or between components of the hydrologic cycle, is characterised by both the ratio and rate of the transfer process (Bracken et al., 2013). Over the past decades, climate change and anthropogenic activities have profoundly altered this connectivity. Specifically, climate warming increases atmospheric moisture-holding capacity and enhances vertical transport and convective rates of water vapour (Ohmura and Wild, 2002; Zhang et al., 2020), leading to more frequent and intense extreme precipitation and consequently elevating flood risks (Yin et al., 2018; Zhang et al., 2023). From precipitation to the runoff generation process, warming significantly alters snowpack dynamics by decreasing the proportion of precipitation being stored as snowpack, along with a faster melting rate (Ombadi et al., 2023). This shifts the seasonal runoff pattern, causing earlier and sharper spring peaks followed by the reduced summer baseflow, which exacerbates agricultural drought and water scarcity in downstream regions (Han et al., 2024). Besides, human activities in urbanisation not only significantly increase precipitation-runoff transformation ratios by expanding impervious surfaces and reducing infiltration, but also shorten the flow concentration time through channel modifications and drainage network construction (Fidal and Kjeldsen, 2020; Barron et al., 2011). These alterations collectively result in flash floods with higher peaks, larger volumes, and earlier arrival times, substantially increasing flood hazards and socioeconomic risks (Blöschl, 2022; Miller and Hess, 2017). Therefore, understanding the process connectivity of the runoff generation is critical for climate adaptation and mitigating water-related hazards.

For quantifying the process connectivity in runoff generation, the most common indicator is the runoff coefficient (*RC*), defined as the volume ratio of precipitation to runoff (Viglione et al., 2009). While the concept of *RC* originates from Sherman (1932), investigations into controls on its spatiotemporal variability are still active in hydrology (Massari et al., 2023; Viglione et al., 2009). The majority of existing research concentrates on small scales, such as agricultural irrigation plots (Badoux et al., 2006; Taye et al., 2013; Sumner et al., 1996; Nyssen et al., 2010) and hillslopes (Kinnell, 2014; Gomi et al., 2008b; Penna et al., 2011; Gomi et al., 2008a). These investigations reveal that the spatial variability of *RC* could be attributed to the spatial pattern of saturated conductivity (Bush et al., 2020; Sheldon and Fiedler, 2008), land degradation (Bush et al., 2020; Sadeghi et al., 2020), land use and cover (Bush et al., 2020; Ziegler et al., 2007), within-plot heterogeneity in soil characteristics (Herbst et al., 2006; Kuhn and Yair, 2004), and interactions among these factors (Li et al., 2025; Xiao et al., 2025). Several studies further investigated the temporal dynamics of the spatial pattern for *RC* across events and found that the spatial pattern may not persist over time (Jiang et al., 2023; Chen et al., 2019; López-Vicente et al., 2016). However, partly owing to the scale dependency of hydrological laws (Oda et al., 2024; Hunt et al., 2025), it is often problematic to extrapolate the discoveries derived from small-scale investigations to larger catchments. Scientific endeavours analysing the *RC* at catchment scale are therefore necessary and crucial.

At the catchment scale, several studies have explored the spatial-temporal variability and influencing factors of *RC* across diverse climates and catchments. These studies indicate a wide range of factors, and their effects differ across various locations. A classical regional analysis of more than 400 Austrian catchments showed that climatic attributes, particularly mean annual precipitation, exert a dominant control on the spatial distribution of *RC* (Merz and Blöschl, 2009). These findings have also been confirmed by other regional studies in Australia and Italy (Norbiato et al., 2009; Wasko and Guo, 2022). In contrast, a large-sample study in the United Kingdom demonstrated that geology and soil properties are important factors of the spatial variability of *RC*. And this is also emphasised by Tarasova et al. (2018) in their analysis of German catchments. For the temporal variations, studies reveal that event rainfall or snowmelt volume, and antecedent soil moisture are the dominant influencing factors (Wu et al., 2021; Merz et al., 2006; Tarasova et al., 2018). Despite these regional investigations, current understanding of the spatiotemporal dynamics of *RC* across diverse regions globally remains few. A broader and more diverse set of catchments and climatic conditions are still required for more comprehensive analyses and reliable findings. Furthermore, *RC* only describes the fraction of precipitation that is transformed into runoff while it cannot reflect how fast this transformation proceeds. This limits our comprehensive understanding of the process connectivity in runoff generation.

To address this limitation, we propose a systematic framework to assess the process connectivity in runoff generation through intensity integration. The *RC* and runoff intensity (i.e., the runoff depth divided by the net-rainfall duration) can reflect the transformation ratio and the rate from precipitation to runoff, respectively. A composite metric, runoff efficiency, is developed to characterise the process connectivity in both dimensions. Applying this framework in 6,603 catchments worldwide over 1950–2020, we quantify the spatial patterns of the process connectivity, diagnose their climatic and landscape controls through the interpretable machine learning, and examine their long-term trends and the event-scale responses to precipitation intensity. The proposed framework will help us understand the precipitation-runoff transformation process across the globe.

2 Methods

To obtain the connectivity indicators for runoff generation, a conceptual hydrological model to simulate the quickflow is first constructed, and then the rainfall-runoff events are identified. Finally, the spatio-temporal variability of these indicators is analysed using interpretable machine learning, Sen's slope, and function fitting approaches. The workflow of this study is presented in Fig. 1.

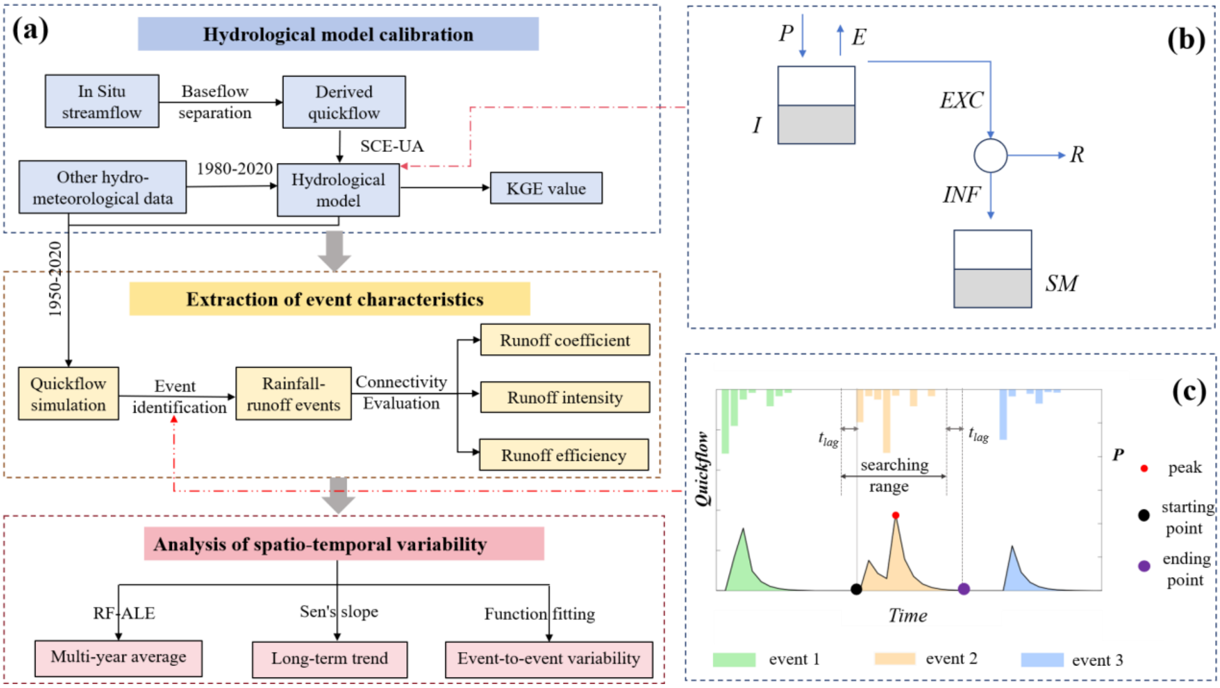

Figure 1. The workflow of this study. (**a**) General framework. (**b**) Structure of the conceptual hydrological model. (**c**) Identification of rainfall-runoff event.

3.1 Quantification of the Process Connectivity in Runoff Generation

3.1.1 Hydrological modeling

As the event runoff-generation process relates to direct runoff (i.e., quickflow), we first separate the baseflow from the observed daily streamflow and then derive the direct-runoff component before running the hydrological modeling (Merz et al., 2006). The baseflow separation is performed using the one-parameter filter approach (Lyne and Hollick, 1979), a method that has been extensively employed in hydrological studies (Mei et al., 2024; Xie et al., 2024; Zhang et al., 2022). To simulate the direct runoff process, we develop a conceptual rainfall–runoff model according to the initial-loss and the continuing-loss framework (O'shea et al., 2021), aiming to represent the Interception and Infiltration processes (Fig. 1b). The Interception by vegetation in the hydrological modeling can be described as:

$$\frac{dI}{dt} = P - E_i - EXC \tag{1}$$

where P (mm/day) represents the liquid-water input, that is, the sum of daily rainfall and snowmelt, making it applicable to the snow-influenced catchments; I (mm) refers to the current interception storage; E (mm/day) and EXC (mm/day) correspond to the evaporation from the interception store and the excess rainfall, respectively. Evaporation is assumed to occur at the potential rate E_p (mm/day) when possible. Once I surpasses the maximum interception capacity I_{max}, the surplus water is routed into the remainder of the model as excess input EXC.

$$E = \begin{cases} E_P, & if \;\; I > 0 \\ 0, & otherwise \end{cases} \tag{2}$$

$$EXC = \begin{cases} P, & if \;\; I = I_{max} \\ 0, & otherwise \end{cases} \tag{3}$$

The subsequent infiltration processes can be described as:

$$INF = f_{max} * SM^b \tag{4}$$

where INF (mm/day) represents the infiltration rate, determined by the maximum infiltration rate f_{max}, soil moisture SM (%), and the infiltration exponent b. The surface runoff (R; mm/day) occurs once the excess rainfall intensity surpasses the infiltration rate of the soil:

$$R = max\,(EXC - INF, 0) \tag{5}$$

The runoff routing is simulated through the classical Nash instantaneous unit hydrograph (Nash, 1957), with two parameters n and K. The parameters n and K are the number of linear reservoirs and the routing time, respectively. All five parameters of the hydrological model (as listed in Table 1) are optimized by the Shuffled Complex Evolution algorithm (SCE-UA), which is a widely adopted stochastic optimization technique for model calibration and parameter tuning (Duan et al., 1992). To ensure a global search of the parameter space for the hydrological model, multiple simplexes are utilized to explore potential solutions concurrently (Kang et al., 2023). The Kling–Gupta Efficiency (KGE) is employed as the objective function:

$$KGE = 1 - \sqrt{(r-1)^2 + (\alpha-1)^2 + (\beta-1)^2} \tag{6}$$

where r represents the correlation coefficient between the simulated and observed values; α denotes the ratio of the standard deviation of simulated results to that of observations; and β indicates the ratio of the mean value of simulated to that of observed streamflow. The calibration and validation of the hydrological model follow the cross-validation technique recommended by Arsenault et al. (2017) and Yin et al. (2021), in which odd-numbered years are chosen for calibration and even-numbered years for validation, with the first two years serving as the model warm-up period. Catchments with KGE values higher than 0.5 during the validation period are retained for further analysis, and their hydrological processes are subsequently simulated over the full 1950–2020 period.

Table 1. Parameters of the hydrological model.

Parameter	Unit	Description
$I_{\max}$	mm	Maximum interception capacity
$f_{\max}$	mm/day	Maximum infiltration rate
b	—	Infiltration exponent
n	—	Number of the linear reservoirs in series
K	day	Routing time parameter

3.1.2 Identification of Rainfall-Runoff Events

We first identify runoff events using the simulated quickflow time series, and then match them to their corresponding rainfall (snowmelt) events. To identify runoff events, following the procedure described by Wu et al. (2021), each quickflow time series is examined starting from the highest peak and then moving to the second-highest peak. The onset of a runoff event is defined as the closest time prior to the peak when quickflow is equal to zero, and the termination is the first time thereafter when quickflow returns to zero, as shown in Fig. 1c. This definition allows multiple peaks to occur within a single runoff event. We then match each identified runoff event with contributing rainfall (including snowmelt) events. Rainfall (snowmelt) events are defined as periods of rainfall that are separated by no-rainfall periods, with a distinguished threshold of 0.1 mm d^{-1} to remove trace or inconsequential events (Wu et al., 2021). For each runoff event in the time series, the total rainfall (or snowmelt) of all events whose centroids lie within a specified range is assigned as the corresponding event rainfall, as illustrated in Fig. 1c. The range refers to the lag time of catchments in event runoff generation, and is determined by a detrending moving-average cross-correlation method (Giani et al., 2021), which as been extensively utilized in hydrology due to its independence from event selection and parameter estimation (Zheng et al., 2023b; Costabile et al., 2024; Zhang et al., 2022).

3.1.3 Evaluation of process connectivity for runoff generation

We first evaluate the process connectivity for runoff generation from the transformation ratio of rainfall to runoff (i.e., runoff coefficient, *RC*) and the transformation rate (i.e., runoff intensity, *RI*), respectively, as follows:

$$RC = \frac{R}{P} \tag{7}$$

$$RI = \frac{R}{\Delta t_R} \tag{8}$$

where *R* denotes the event runoff depth, and *P* refers to the event rainfall (including the snowmelt) depth. Δt_R is the event runoff duration (i.e., the net-rainfall duration), defined as the time during which $R > 0$ within an event, distinct from the event rainfall period. Thus, Δt_R is expected to be shorter than the precipitation duration because of interception, infiltration, and other losses in runoff generation (Gyasi-Agyei and Melching, 2012; Hashino et al., 2002). The higher the *RC*, the higher the transformation ratio in runoff generation. The greater the *RI*, the faster the transformation rate.

To comprehensively characterise the process connectivity of the two aspects, we further define runoff efficiency (*RE*) to be the product of *RC* and *RI*:

$$RE = RC * RI \tag{9}$$

The higher the *RE* value is, the larger fraction is transformed to runoff with a faster rate for a given precipitation input within an event. Typically, it is associated with a larger event runoff volume and higher peak discharge, and thus a greater flood risk.

3.2 Analysis of spatio-temporal variability for process connectivity

3.2.1 Analysis of multi-year average

Random Forest (RF)-accumulated local effects (ALE) are employed as an interpretable machine learning approach to explore the spatial patterns of RCs. The Random Forest (RF) represents a traditional machine learning approach constructing an ensemble of regression trees (Breiman, 2001). Compared with single regression tree algorithms, RF provides notable strengths, such as the ability to manage highly correlated input variables, capture nonlinear interactions, and improve predictive stability via ensemble aggregation. The RF approach has been extensively utilized across diverse hydrological applications (Zheng et al., 2023a; Brown et al., 2023; Stein et al., 2021). The input features of the RF involve four categories of catchment characteristics: climate, topography, soil, and land cover (Zheng et al., 2023a; Kemter et al., 2023). To avoid the redundancy of the input features, following Brêda et al. (2024) and Liang et al. (2026), catchment attributes with the Pearson correlation coefficient above 0.75 among various groups and above 0.9 within the same group have been removed (Fig. S1). Ultimately, 22 catchment variables spanning the four categories were retained, with detailed descriptions provided in Table. S1. To avoid overfitting of RF, a 10-fold cross-validation strategy is adopted in evaluating the performance (Stein et al., 2021). The dataset is partitioned into ten subsets of equal size. Nine of the subsets are adopted to train the RF, while the left is for testing. The coefficient of determination (R^2) is employed as a metric for the performance of RF. Model robustness is examined by performing 100 independent iterations of RF training with varying random seeds. The overall performance of the RF model is summarized by the average R^2 obtained across all 100 iterations.

To quantify the average effects of the inputs on the performance of the RF, the ALE is adopted (Apley and Zhu, 2020). As a model-agnostic technique, ALE extends the concept of partial dependence plots, and provides improved computational efficiency and reliability, especially when predictors are correlated or data exhibit complex structures (Shelef et al., 2022; Kemter et al., 2023). Its robustness stems from focusing on localized variations around observed values rather than the entire predictor range. By concentrating on the empirical distribution of the data, ALE estimates the causal influence of inputs on predictions while reducing extrapolation errors, thereby improving interpretability. To quantify the primary effect of a predictor, the uncentred effect $\hat{g}_{j,\mathrm{ALE}}(x)$ is determined by the differences of the predictions from the quantiles of the predictor as indicated in Equation (10) (Apley and Zhu, 2020).

$$\hat{g}_{j,\mathrm{ALE}}(x) = \sum_{m=1}^{M} \frac{1}{n_j(m)} \sum_{\{i: x_{i,j} \in N_j(m)\}} \{g(z_{m,j}, \mathrm{x}_{i,\setminus j}) - g(z_{m-1,j}, \mathrm{x}_{i,\setminus j})\} \qquad (10)$$

where x refers to a given value of predictor j used in calculating the ALE plot; m corresponds to a specific quantile within the set of M quantiles ($M = 10$) that subdivide the range of x. The range is partitioned into ten equal intervals for a balance between result robustness and low computational cost. The term $n_j(m)$ refers to the number of values of x that lie in the mth interval $N_j(m)$ ranging from $i = 1, 2, \ldots n$, and n represents the total sample size; $z_{m,j}$ refers to the boundary value of x for the given quantile; $g(\cdot)$ denotes the prediction model output, and $x_{i,\setminus j}$ corresponds to the values of all other predictors for instance i except predictor j. The primary effect estimator $\hat{f}_{j,\mathrm{ALE}}(x)$ of the ALE can be further estimated through deducting the average for uncentred effect value of all quantiles:

$$\hat{f}_{j,\mathrm{ALE}}(x) = \hat{g}_{j,\mathrm{ALE}}(x) - \frac{1}{M_j} \sum_{m=1}^{M} \hat{g}_{j,\mathrm{ALE}}(x_m) \, . \qquad (11)$$

To represent the contribution of each predictor, the average absolute values of ALE are obtained and normalised (maximum-minimum normalisation) into the 0-1 range for comparability (Stein et al., 2021)

3.2.2 Analysis of long-term trend

To explore the long-term evolution of process connectivity indicators, we use Sen's slope, a robust and nonparametric method, to detect temporal trends, which is commonly used in hydro-meteorological research to estimate linear trends (Bloeschl et al., 2019; Kemter et al., 2023; Wang et al., 2024).

$$k = median\left(\frac{Y_j - Y_i}{j - i}\right) \qquad (12)$$

where k is the slope; Y denotes the process connectivity indicator; i and j ($i < j$) are all possible pairs of years within the time series.

3.2.3 Analysis of event-to-event variability

For each catchment, we first examine how process-connectivity indicators varied across events that are grouped by different discharge quantile intervals. Besides, we analyse the effect of precipitation intensity on runoff efficiency across events by fitting a power function based on the least squares method. The power function is chosen due to its universality in numerous hydrological formulas (Ijjaszvasquez et al., 1992; Schwemmle and Weiler, 2024; Li and Sivapalan, 2011).

$$RE = RE_{10} * \left(\frac{PI}{10}\right)^{m} \qquad (13)$$

where PI represents the precipitation intensity. RE_{10} and m are the fitted parameters. The former denotes the runoff efficiency at a unit precipitation intensity (10mm/day), and the latter indicates the sensitivity.

3 Data

The hydrological and meteorological data come from the Caravan large sample dataset (Färber et al., 2025; Kratzert et al., 2023), which compiles time series and catchment attributes for over 20,000 catchments worldwide. Specifically, daily observed discharge (Q) is sourced from gauge stations, while precipitation (P), temperature (T), soil moisture (SM), and snow water equivalent (SWE) are sourced from ERA5-Land. The potential evapotranspiration (PET) is estimated by the FAO Penman–Monteith equation. All meteorological data have been aggregated to the catchment scale. We applied the following criteria to select catchments. First, catchments are required to have a minimum of 20 years of observed Q records between 1980 and 2020, with no data gaps exceeding 10 days; any remaining missing values are imputed using linear interpolation (Jiang et al., 2024). Then, catchments with poor performance for hydrological simulation (See section 2.1), indicated by a Kling-Gupta efficiency (KGE) value lower than 0.5, are filtered out. These criteria screen a total of 6603 catchments for analysis.

To investigate the differences across climates, catchments are classified into three climatic categories: wet, dry, and snow. Wet catchments are characterized by an aridity index below 1, where mean potential evapotranspiration is lower than precipitation, indicating energy-limited conditions. Dry catchments correspond to an aridity index exceeding 1, in which mean potential evapotranspiration surpasses precipitation, reflecting water-limited conditions. Snow-dominated catchments are identified by a snow fraction greater than 0.2, independent of the aridity index (Wang et al., 2024; Stein et al., 2021). To highlight regional characteristics, the catchments are also grouped into 14 IPCC reference regions, with each region containing more than 30 catchments (Iturbide et al., 2020). The distribution of catchments is illustrated in Fig. 2.

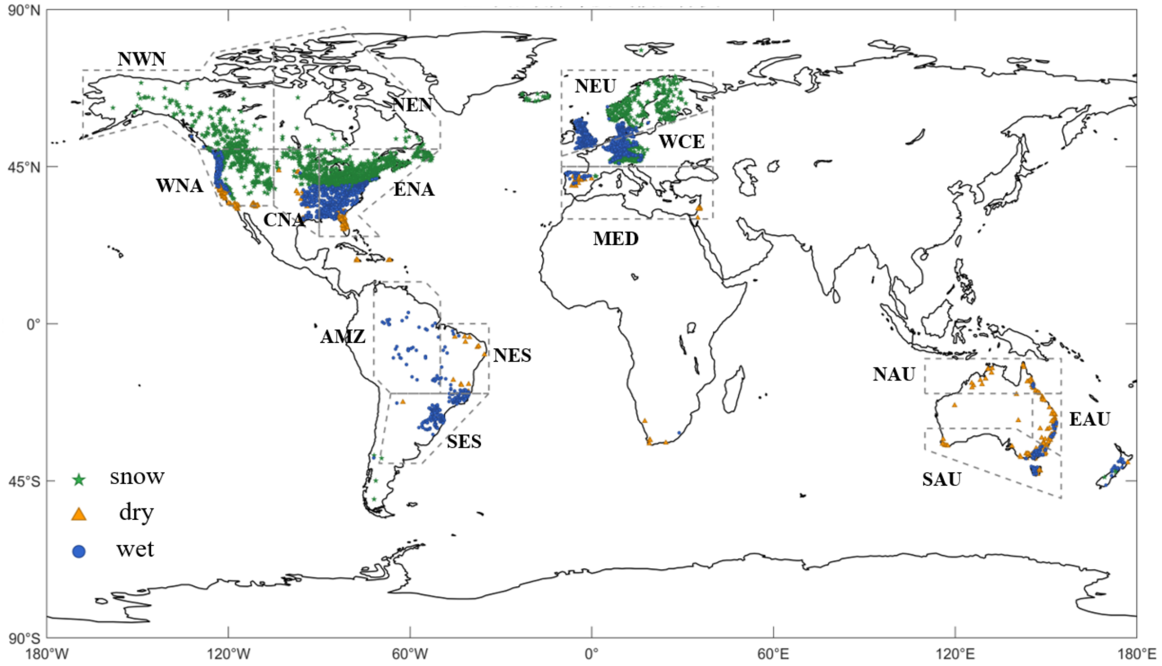

Figure 2. Spatial distribution of 6603 catchments for analysis. The green stars, orange triangles, and blue circles indicate the catchments in snow, dry, and wet climate zones, respectively. AMZ, Amazon; CNA, central North America; EAU, eastern Australia; ENA, eastern North America; MED, Mediterranean; NAU, northern Australia; NEN, north-eastern North America; NEU, northern Europe; NES, northeastern South America; NWN, northwestern North America; SAU, southern Australia; SES, southeastern South America; WCE, western and central Europe; WNA, western North America.

4 Results

4.1 Spatial Patterns of Process Connectivity and Influencing Factors

A total of 2,553,834 rainfall-runoff events from 1950 to 2020 in 6603 catchments are identified according to the simulation of conceptual hydrological model. The mean value of each connectivity indicator across all events is determined, and its spatial pattern for the multi-year average is illustrated in Fig. 3. For the runoff coefficient (Figs. 3a-c), the dry climates are found to have the lowest value, with a median of 0.15, indicating a high loss in the transformation process from precipitation to runoff. In contrast, the wet and snow climates have relatively higher values, with a median of 0.25 and 0.33, respectively, indicating a lower loss in the transformation process. It is also interesting that the highest values are found in western North America (WNA) and northwestern North America (NWN), with a median higher than 0.3, while the lowest values are found in eastern Australia (EAU), northeastern South America (NES), and southern Australia (SAU), with a median lower than 0.15.

However, in terms of the runoff intensity as shown in Figs.3d-f, the highest value can be found in the dry climate zones, with a median of 11.3mm/day. Thus, there is a high rate in the transformation process from precipitation to runoff. In contrast, the relatively lower values are found in the wet and snow climate zones, with a median of 8.6mm/day and 8.5mm/day, respectively, indicating a lower rate in the transformation process. From the spatial distribution, the highest values of runoff intensity are found in the eastern Australia (EAU), northeastern South America (NES), and northern Australia (NAU), with a median higher than 12mm/day, while the lowest values are found in northern Europe (NEU), northwestern North America (NWN), and Mediterranean (MED), with a median lower than 6.5mm/day. It should be noted that the spatial pattern of runoff coefficient is not consistent with that of runoff intensity. For example, NWN exhibits a relatively high runoff coefficient of 0.3 but a comparatively low runoff intensity of 6.5 mm/day.

In terms of the runoff efficiency as shown in Figs. 3g-i, which is the product of the runoff coefficient and runoff intensity, its relatively high values are found in snow climates with median=2.41mm/day, and a lower value is found in both wet (median=1.75mm/day) and dry (median=1.51mm/day) climates, indicating a balance between runoff coefficient and runoff intensity. Its spatial distribution is different from that of the runoff coefficient and the runoff intensity. The highest values of the runoff efficiency are found in western North America (WNA), eastern North America (ENA), and southeastern South America (SES), with a median higher than 2.5 mm/day, indicating a larger fraction of rainfall transformed to runoff with a faster rate, typically associated with a larger event runoff volume and higher peak discharge, and thus a greater flood risk. In contrast, the lowest values of the runoff efficiency are found in southern Australia (SAU), northern Europe (NEU), and northeastern South America (NES), with a median lower than 1.35 mm/day, suggesting a lower comprehensive connectivity for runoff generation, and thus a lower flood risk.

The interpretable machine-learning framework combining RF and ALE is subsequently employed to investigate the drivers controlling the spatial heterogeneity of the process connectivity indicators described above. The 22 catchment attributes serve as inputs in the RF model for predicting each process connectivity metric. The cross-validated R^2 values for the RF models are presented in Figs. S2-S4. Generally, the RF model shows a great performance, with the mean R^2 over 0.82 for all indicators in 10-fold cross-validation. Figure 4 illustrates the ALE interpretable results of each indicator. For the runoff coefficient as shown in Fig. 4a, the aridity is the greatest impact indicator, followed by mean annual precipitation, organic carbon content in soil, seasonality of precipitation, and fraction of snow. In terms of the runoff intensity as shown in Fig. 4b, the mean annual precipitation has the greatest impact, followed by the mean actual evapotranspiration, the average duration of high precipitation, and the frequency of high precipitation days. In terms of the runoff efficiency as shown in Fig. 4c, the greatest impact indicator is the mean annual precipitation, followed by the frequency of high precipitation days, seasonality of precipitation, fraction of snow, and pasture extent. It can be noted that climate attributes dominate the influence on all connectivity metrics, contributing 61.8%, 88.2%, and 77.0% to the runoff coefficient, runoff intensity, and runoff efficiency, respectively.

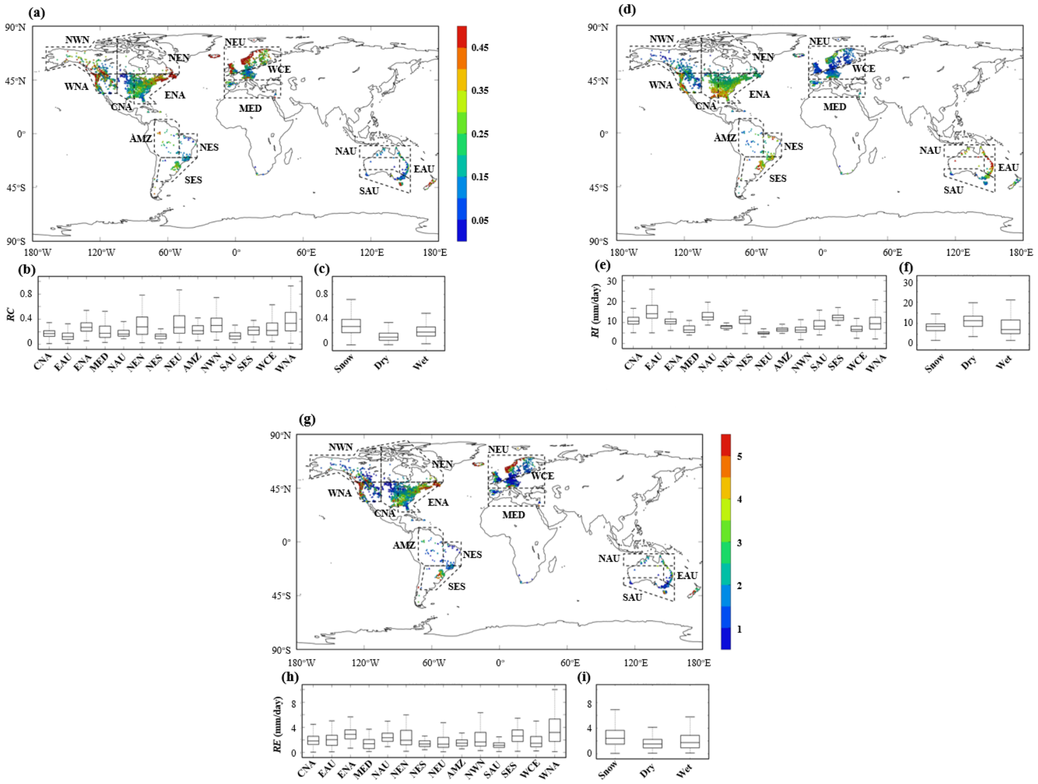

Figure 3. The spatial pattern for the multi-year average of the process connectivity indicators across the globe. (**a-c**) for the runoff coefficient. (**d-f**) for the runoff intensity. (**g-i**) for the runoff efficiency.

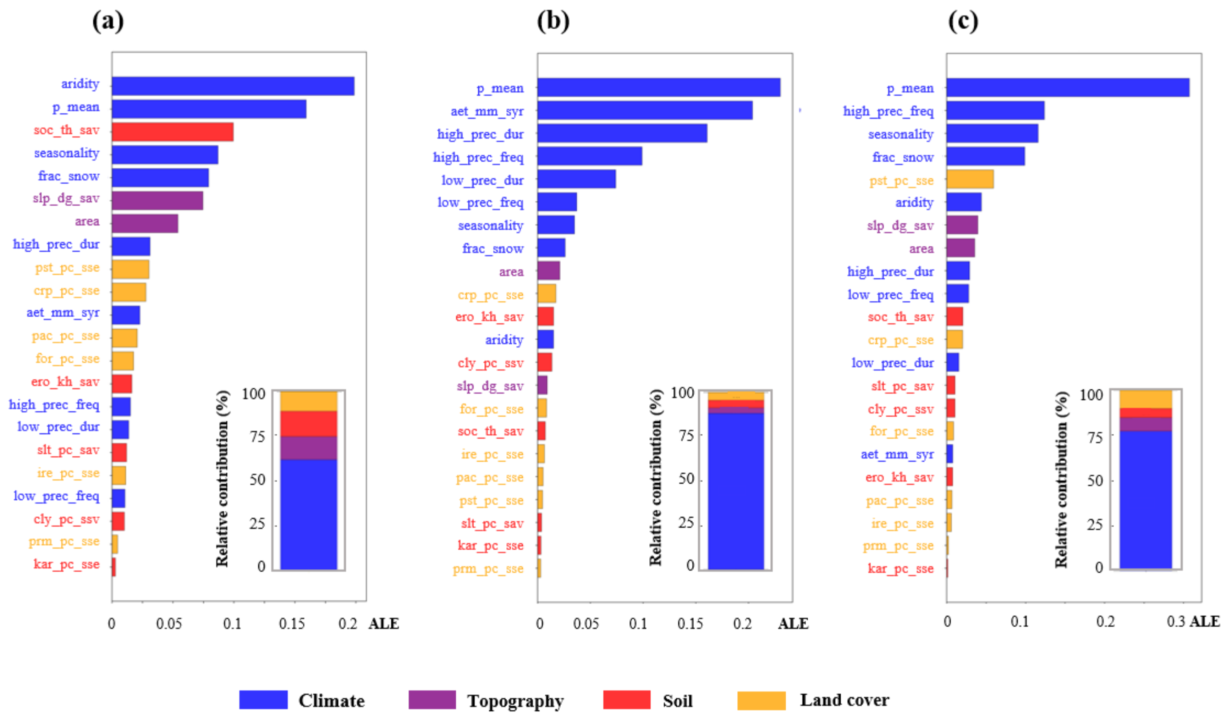

Figure 4. The Influence of catchment attributes on process connectivity indicators based on the interpretable machine learning approach (RF-ALE). (**a**) runoff coefficient. (**b**) runoff intensity. (**c**) runoff efficiency. Blue, purple, red, and yellow correspond to the categories of catchment attributes related to climate, topography, soil properties, and land cover, respectively. The proportional contribution of each category is illustrated by the bar height in the lower-right corner.

4.2 Long-Term Trends of Process Connectivity

Figure 5 illustrates the long-term trends of process connectivity from 1950 to 2020. In terms of the runoff coefficient as shown in Figs.5a-c, the increasing trends are found in most catchments in dry and wet climate zones, with a median relative Sen's slope of 0.6%/decade and 0.3%/decade, respectively. In contrast, most catchments in snow climates exhibit declining trends, with a median relative Sen's slope of -0.2%/decade. The high increasing trends are mainly located in the Amazon (AMZ; 1.6%/decade), northern Australia (NAU, 1.2%/decade), central North America (CNA; 1.2%/decade), southeastern South America (SES, 1.1%/decade), and northeastern South America (NES, 1.0%/decade). Besides, the high decreasing trends mainly lie in the Mediterranean (MED, -1.0%/decade) and western North America (WNA, -0.6%/decade). For the runoff intensity (Figs. 5e-f), the spatial pattern of long-term trends resembles that of the runoff coefficient, with the high increasing trends in the AMZ (2.6%/decade), SES (2.0%/decade), NES (1.9%/decade), NAU (1.8%/decade) and CNA (1.4 %/decade), and the high decreasing trends in WNA (-0.9%/decade) and MED (-0.7%/decade). This indicates that long-term trends of the transformation rate (i.e., runoff coefficient) and the transformation rate (i.e., runoff intensity) from precipitation to runoff show great synergy, meaning that regions with a higher transformation rate may simultaneously mean a faster transformation rate under climate change. In term of runoff efficiency as shwn in Figs.5g-i, the high increasing trends also lie in the AMZ (3.4%/decade), SES (2.5%/decade), CNA (2.3%/decade), NAU (1.8%/decade), and NES (3.0%/decade), and the high decreasing trends are also in the WNA (-1.5 %/decade) and MED (-0.9 %/decade), while the changing amplitude is greater than that of the runoff coefficient and runoff intensity.

Generally, the hotspots of increasing process connectivity for runoff generation under climate change are the Amazon, southeastern South America, central North America, northern Australia, and northeastern South America, with a larger fraction of rainfall transformed to runoff with a faster rate, typically associated with a larger event runoff volume and higher peak discharge, and thus a greater flood risk. Besides, the hotspots of decreasing process connectivity are western North America and the Mediterranean, with relatively lower flood risk.

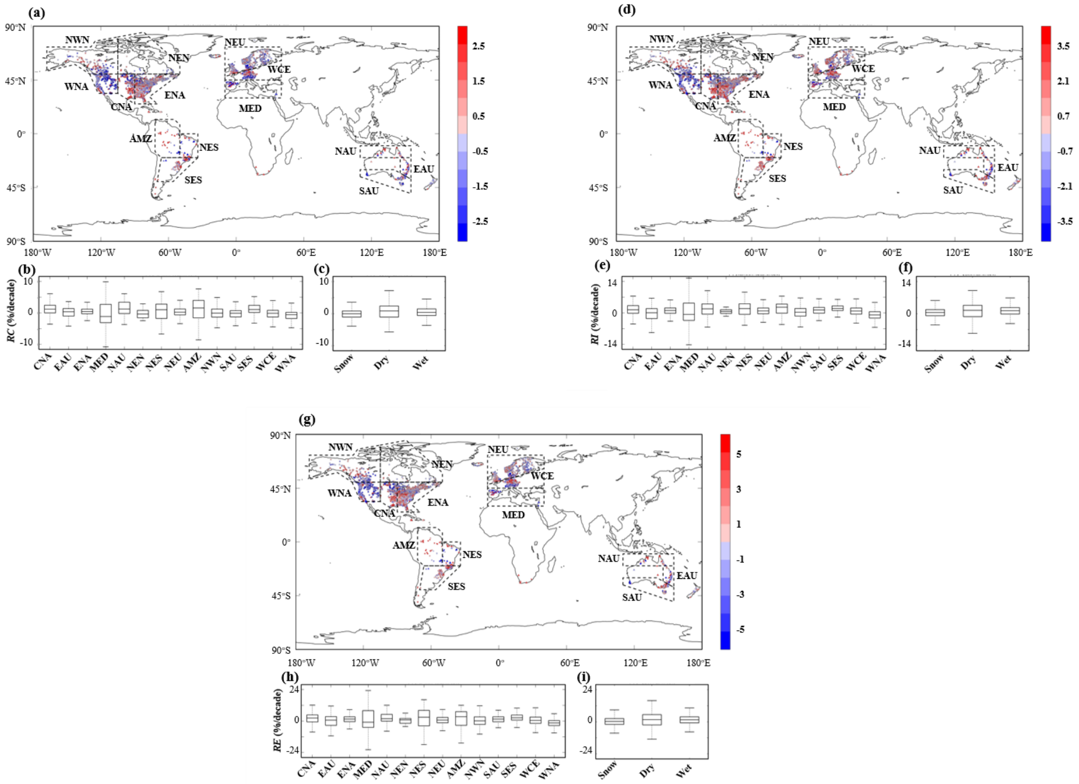

Figure 5. The long-term trends of the process connectivity indicators over 1950-2020. (**a-c**) for the runoff coefficient. (**d-f**) for the runoff intensity. (**g-i**) for the runoff efficiency.

4.3 Event-To-Event Variability of Process Connectivity

By examining the differences in process connectivity indicators among events grouped by peak discharge quantile ranges (Figs. S5-S7), we find that the connectivity indicators increase with the discharge quantiles, demonstrating the strong association between process connectivity of runoff generation and the peak discharge of events. To contrast the extremes, we further calculated the fold-change in the connectivity indicators from the highest to the lowest peak-discharge quantile ranges, i.e., (80–100th percentile)/ (0–20th percentile), as shown in Fig. 6. In general, across all catchments, the runoff coefficient, runoff intensity, and runoff efficiency for events with large peak discharge quantiles are 3, 4, and 11 times those with small peak discharge quantiles, respectively. For the runoff coefficient (Figs. 6a-c), the highest ratios are found in the dry climate zones, with a median value of 5.4, while wet and snow climates have relatively lower values, with a median value of 3.5 and 2.7, respectively. In spatial distribution, the high values are found in EAU, NAU, CNA, and SAU, with a median value of 6.6, 4.8, 4.1, and 4.1, respectively, while the low values are found in NEN, NWN, and AMZ, with a median value of 1.6, 1.9, and 2.5. For the runoff intensity and runoff efficiency as shown in Figs. 6d-i, the spatial distribution is similar to that of the runoff coefficient, with the high values in EAU(17.1;87.3), NAU(11.5; 46.5), CNA(8.0;27.5), and SAU(6.7;21.9), and low values in NEN (2.3;2.9), NWN (2,2;3.6), and AMZ (1.9;3.6) for both indicators. Besides, the highest ratios are found in the dry climates, with 10.7 and 54.4 times for runoff intensity and runoff efficiency, suggesting significant nonlinear characteristics.

To investigate the effect of precipitation intensity on runoff efficiency, we adopted a power function to fit for each catchment across all events based on the least squares method. The fitting example is illustrated in Fig. S8, and the fitting performance for all catchments is presented in Fig. S9, with a mean R^2 of 0.37. The spatial pattern of the fitted parameters RE_{10} and m is presented in Fig. 7, and their regional statistics are summarised in Table 2. For RE_{10} (Figs. 7a-c), representing the runoff efficiency at a unit precipitation intensity (10mm/day), its spatial pattern resembles that of multi-year average runoff efficiency (Fig. 4c). The relatively lower values are found in dry climate zones, with a median of 1.9mm/day, while the relatively higher values are found in the wet and snow climate zones, with a median of 2.8mm/day and 3.8mm/day, respectively. Regionally, the highest values (i.e., 3.9mm/day) are found in NEN and WNA, while the lowest values (0.9mm/day) are found in EAU. The parameter m, as shown in Figs. 7d-f reflects the sensitivity of runoff efficiency to precipitation intensity. Its highest value, with a median of 1.65, is found in the dry climate zones, while the relatively lower values, with a median of 1.17 and 1.05, are found in the wet and snow climate zones, respectively. Thus, the relatively low RE_{10} values are associated with high sensitivity for dry climate zones, and the relatively high RE_{10} values are associated with low sensitivity for wet and snow climates. Regionally, the highest sensitivities are found in EAU (1.88) and NAU (1.70), while the lowest sensitivities are found in MED (0.67) and NEN (0.72).

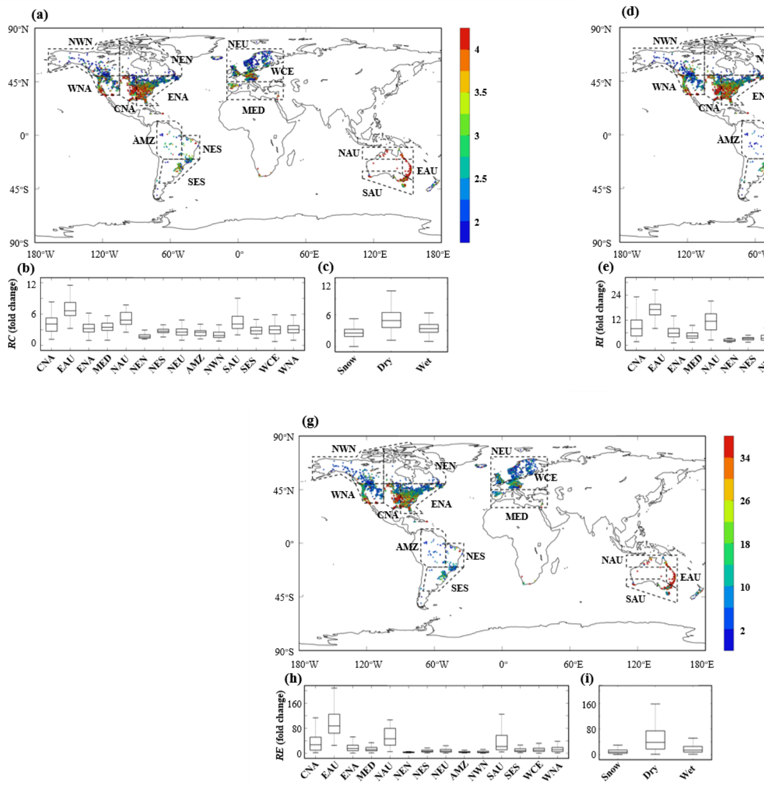

Figure 6. The fold-change in the connectivity indicators from the highest to the lowest peak-discharge quantile ranges, i.e., (80–100th percentile)/ (0–20th percentile). (**a-c**) for the runoff coefficient. (**d-f**) for the runoff intensity. (**g-i**) for the runoff efficiency.

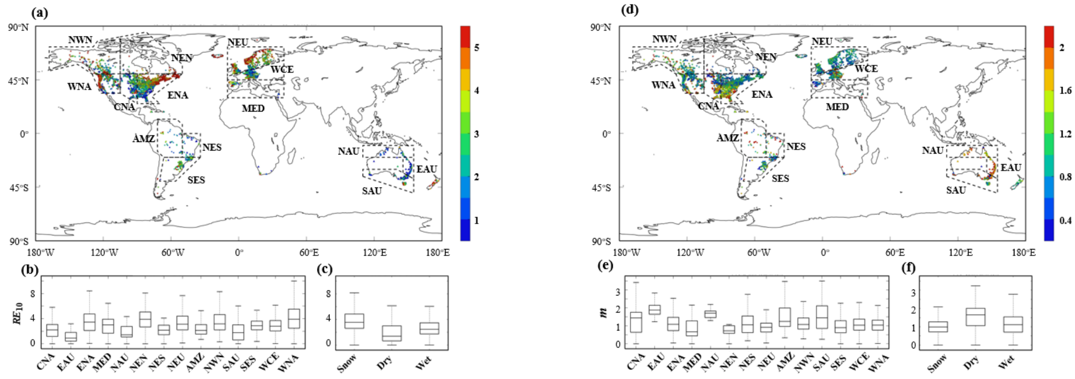

Figure 7. The spatial pattern of parameters of the power-law relationships between precipitation intensity and runoff efficiency. (**a-c**) for the parameter RE_{10}. (**d-f**) for the parameter *m*.

https://doi.org/10.5194/egusphere-2026-1006
Preprint. Discussion started: 4 March 2026

Table 2. Parameters and determination coefficients (R^2) of the power-law relationships between precipitation intensity and runoff efficiency across regions.

Region	CNA	EAU	ENA	MED	NAU	NEN	NES	NEU	AMZ	NWN	SAU	SES	WCE	WNA
RE_{10}	2.21	0.90	3.45	3.00	1.43	3.90	2.16	3.12	2.12	3.17	1.77	2.88	2.80	3.91
m	1.44	1.88	1.09	0.67	1.70	0.72	1.06	0.92	1.25	1.08	1.45	0.90	1.04	1.04
R^2	0.36	0.69	0.36	0.22	0.67	0.38	0.34	0.37	0.37	0.44	0.37	0.25	0.34	0.44

5 Discussion

Using the interpretable machine learning method, we revealed the factors influencing the spatial variability of the process connectivity indicators across the globe (Fig. 4). For the runoff coefficient (*RC*), the dominant factors are aridity and mean annual precipitation. This finding aligns with previous regional investigations, which demonstrated that mean runoff coefficients are primarily governed by climatic factors, particularly the multi-year average of precipitation and the ratio of evapotranspiration to precipitation (Merz and Blöschl, 2009; Merz et al., 2006). Thus the climatic water–energy balance largely determines the average fraction of precipitation that becomes runoff, in line with the classical Budyko framework that a higher climatic aridity index increases the evaporative fraction (E/P) and reduces the runoff coefficient, leading to low runoff coefficients in dry areas and higher runoff coefficients in wet areas (Liang et al., 2015; Cheng et al., 2025; Cavalcante et al., 2019). In terms of runoff intensity (*RI*), the dominant factors are the average duration and frequency of high-precipitation events, highlighting the transfer of the temporal characteristics from precipitation to runoff generation. For the runoff efficiency (*RE*), the dominant factors are the multi-year average of precipitation, frequency of high-precipitation events, and seasonality of precipitation, indicating the rationality of this integrated connectivity metric that can capture both dimensions of quantity and speed for runoff generation. In terms of categorical attributions, the explainable machine learning indicates that climatic indicators control the process connectivity at the global scale, whereas landscape characteristics, including topography, soil properties, and land cover, exert a comparatively limited influence. These findings are consistent with previous work on the controls of runoff generation, which emphasised the dominance of climate attributes in runoff generation processes (Jehn et al., 2020).

By analysing long-term trends of the connectivity indicators for runoff generation over 1950–2020, we identified several hotspots of evolving flood risk **(**Fig. 5). In general, trends in the *RC* and *RI* are highly coherent across most catchments worldwide, with regions showing increases in transformation ratios tending to exhibit simultaneous increases in transformation intensity, and vice versa. Under the changing climate, the Amazon, southeastern and northeastern South America, central North America, and northern Australia show pronounced increases in runoff generation connectivity. This might be attributed to the increases in occurrence frequency and magnitude of extreme precipitation events, which make a larger fraction of precipitation rapidly transformed into runoff (Donat et al., 2016; Harp and Horton, 2022). The increasing connectivity brings larger event runoff volumes and higher peak discharges, and thus potentially causes a greater flood risk. In contrast, the decreasing trends in runoff generation connectivity are found in western North America and the Mediterranean, which might be attributed to the reduction of total precipitation and enhanced evaporation. Thus, there are drier soils, lower runoff coefficients, and weaker runoff intensity, and consequently a reduction in average flood risk (Zhan et al., 2019). It should be noted that a lower connectivity does not imply absolute safety, as extreme events may still occur (Yan et al., 2025). Overall, the trends of the runoff generation connectivity provide a process-based perspective on acceleration or deceleration of the global hydrological cycle and reveal how the spatial pattern of flood risk evolves under climate change.

At the event scale, we established an empirical power-law relationship linking precipitation intensity to runoff efficiency. The relationship is simple and flexible, requiring only two parameters, and can summarise how runoff-generation connectivity responds to precipitation intensity from weak to strong events. Across all catchments, the mean coefficient of determination is around 0.37, indicating that precipitation intensity alone can explain a substantial portion of the variability in runoff efficiency. Analyses across climate conditions show that dry catchments exhibit a low baseline runoff efficiency at a unit precipitation intensity (RE_{10}), while the sensitivity parameter m is the highest **(**Figs. 7c,f). This implies that strong evaporation and infiltration losses keep low runoff-generation connectivity under ordinary storms, whereas sufficiently intense events can temporarily exceed the soil infiltration capacity, causing the amount and intensity of runoff to increase sharply and leading to an amplification effect to precipitation intensity ($m > 1$). In contrast, wet catchments tend to display high RE_{10} but low sensitivity, with small to moderate storms already generating a relatively large fraction of runoff, and further increases in precipitation intensity might not translate into proportional gains in runoff efficiency. This contrast reflects the fundamental differences in runoff-generation mechanisms: runoff generation is typically dominated by infiltration-excess runoff with clear intensity thresholds in dry catchments, whereas it is more prone to saturation-excess runoff in wet catchments, where near-saturated soils allow even modest storms to produce runoff, leading to high baseline efficiency but much smoother changes with intensity. As the precipitation regime is projected to change under future climates (Song et al., 2024; Liu et al., 2024), regional empirical relationships between precipitation intensity and runoff efficiency provide a practical way for assessing shifts in runoff-generation connectivity, with potential applicability across the globe.

Overall, this study proposes an integrated framework for assessing process connectivity that jointly considers both the transformation ratio and rate from precipitation to runoff. In contrast to traditional approaches that only focus on a volumetric transformation ratio through the runoff coefficient, our new set of metrics explicitly separates runoff generation into two dimensions, including quantity and speed. By introducing runoff intensity into the assessment, we overcome the

https://doi.org/10.5194/egusphere-2026-1006
Preprint. Discussion started: 4 March 2026

limitation that a single runoff coefficient cannot describe the velocity characteristics of runoff generation, and further define a comprehensive connectivity metric (i.e., *RE*), thus deepening our process-based understanding of runoff generation. Our results show that *RE* predominantly reflects a trade-off between *RC* and *RI* at the multi-year mean scale spatially. In other words, under long-term average conditions, catchments with high *RC* tend to exhibit relatively low *RI*, and vice versa **(**Fig. 3). This might be attributed to different runoff-generation mechanisms across climates (Stein et al., 2021). For example, in wet or snow conditions, soils are close to saturation, with a large fraction of rainfall or snowmelt transformed to runoff (high *RC*), while the events may last longer, leading to relatively low runoff intensity (low *RI*). In contrast, in dry conditions, short and intense storms produce high runoff intensity (high *RI*), yet a substantial part of the precipitation is lost to infiltration and evaporation, which reduces the runoff coefficient (low *RC*). This contrast highlights the long-term regulatory impact of climatic conditions on process connectivity for runoff generation, that is, water-abundant conditions tend to "win by quantity", whereas water-limited conditions "win by rate", establishing a compensatory balance between *RC* and *RI*. However, in contrast to the long-term trade-off, event-scale *RE* shows a strongly nonlinear response to meteorological forcing, especially a pronounced amplification with increasing precipitation intensity. Specifically, we found that as the intensity of individual precipitation events increases, *RE* grows nonlinearly, with high-intensity storms producing much larger *RE* than low-intensity events **(**Fig. 7). Such behaviour is difficult to detect from long-term averages, where the effects of events with different intensities are smoothed out in time. This nonlinear amplification indicates that, during heavy storms, both the fraction and rate of the transformation from precipitation to runoff increase simultaneously and substantially. This might be attributed to the threshold effect in the precipitation–runoff process. When rainfall intensity is below a certain threshold, most water is intercepted or infiltrated into the soil, limiting hydrologic connectivity and keeping both *RC* and *RI* relatively low. When rainfall intensity surpasses the soil's infiltration capacity or storage thresholds of underlying surface, excess precipitation rapidly produces overland flow, and the runoff connectivity is activated (Zhang et al., 2021). More precipitation could be transformed into runoff with a faster rate, causing a sharp increase in *RE*. Such threshold-triggered nonlinear responses in runoff generation have been reported in many previous studies (Detty and Mcguire, 2010; Mahmood and Vivoni, 2011; Willgoose and Perera, 2001). Therefore, the combined use of *RC*, *RI* and *RE* provides a set of quantitative metrics for characterising the connectivity of the runoff generation, and it can improve our understanding of how the water cycle responds to the changing climate from the process perspective.

It is also worth knowing the limitations of our study. First, we only use a single conceptual rainfall–runoff model, which introduces uncertainty of model structure for global application (Parasuraman and Elshorbagy, 2008). Although parameter calibration and performance screening ensured a reasonable level of accuracy, future work could employ ensembles of hydrological models to represent runoff-generation processes more comprehensively and to enhance the robustness of the results (Solanki et al., 2025). Second, in terms of temporal resolution, we currently use daily meteorological and hydrological data to identify events and compute the metrics. This timescale neglects sub-daily storm dynamics, which are particularly important for metrics that reflect the rate of runoff generation, such as *RI* and *RE*. Extending the framework to higher-frequency hydrometeorological observations, such as hourly precipitation and streamflow, would allow a more detailed characterisation of peak runoff responses and process connectivity. Third, the empirical power-law relationship developed here does not account for antecedent soil moisture. In fact, runoff efficiency relies both on precipitation intensity and antecedent conditions preceding the event (Zhang et al., 2021). Two storms with similar precipitation intensities can produce markedly different runoff efficiencies, with one following a prolonged dry spell generally producing lower efficiency than that occurring under wet antecedent conditions. Since future climate change may alter both the distribution of precipitation intensity and soil moisture (Yao et al., 2025), the empirical relationship calibrated under current conditions remains invalid under future scenarios. These limitations and uncertainties will be addressed in future work.

6 Conclusions

A new framework for assessing process connectivity in runoff generation through intensity integration has been developed. The *RC* and *RI* are adopted to represent the transformation ratio and rate from precipitation to runoff, respectively, and a composite metric *RE* is proposed to characterise process connectivity in both dimensions. Applying this framework to 6,603 catchments globally over 1950–2020, we quantify the spatial patterns of process connectivity, figure out their climatic and landscape controls using interpretable machine learning, and examine their long-term trends and event-scale responses to precipitation intensity. According to the long-term average values of the metrics, we find a relatively high *RC* and *RI* in wet and dry areas, respectively. Interpretable machine learning further reveals that climatic attributes, especially aridity, mean annual precipitation, average duration and frequency of high-precipitation events, and the seasonality of precipitation, primarily control the process connectivity indicators at the global scale. The analysis of long-term trends shows that the hotspots of increasing process connectivity are Amazon, southeastern South America, central North America, northern Australia, and northeastern South America, typically associated with a larger event runoff volume and higher peak discharge, and thus a greater flood risk, while hotspots of decreasing process connectivity are found in western North America and the Mediterranean, with relatively lower flood risk. Event-scale analysis shows that across all catchments, the *RC*, *RI,* and *RE* for events with large peak discharge quantiles are three, four, and 11 times those with small peak discharge quantiles. We further establish an empirical power-law relationship between precipitation intensity and *RE* and find a high sensitivity for dry climates. Overall, our proposed process-connectivity framework, considering both transformation ratio and rate, offers a new perspective to understand spatiotemporal variations in the runoff generation process, and it can be further extended to diagnose other processes in the global hydrological cycle, such as precipitation recycling and runoff routing processes.

Code and data availability

The Caravan dataset (Kratzert et al., 2023) can be accessed publicly via https://zenodo.org/records/7540792. The Random Forest algorithm was implemented using the Python scikit-learn library, which is available at https://scikit-learn.org/stable/. The code for computing accumulated local effects (ALE) can be obtained from https://github.com/DanaJomar/PyALE.

Author contributions

HL designed the model architecture, performed the computations, conducted the statistical analysis, and drafted the manuscript. DL acquired funding, contributed to the study design, provided research data, supervised the project, and guided the manuscript revision. JZ contributed to manuscript revision discussions and provided advice on submission procedures. FY and YZ participated in revision discussions and contributed to figure and chart preparation. All authors reviewed and approved the final version of the manuscript for submission.

Competing interests

The contact author has declared that none of the authors has any competing interests.

Disclaimer

Acknowledgements

The authors gratefully acknowledge the financial support from the National Key Research and Development Project of China (2024YFC3012402) and the National Natural Science Foundation of China (No. 52379022).

Financial support

This research has been supported by the National Key Research and Development Project of China (grant nos. 2024YFC3012402) and the National Natural Science Foundation of China (grant nos. 52379022).

References

Apley, D. W. and Zhu, J. Y.: Visualizing the effects of predictor variables in black box supervised learning models, Journal of the Royal Statistical Society Series B-Statistical Methodology, 82, 1059-1086, https://doi.org/10.1111/rssb.12377, 2020.

Arsenault, R., Essou, G. R. C., and Brissette, F. P.: Improving Hydrological Model Simulations with Combined Multi-Input and Multimodel Averaging Frameworks, J. Hydrol. Eng., 22, https://doi.org/10.1061/(asce)he.1943-5584.0001489, 2017.

Badoux, A., Witzig, J., Germann, P. F., Kienholz, H., Lüscher, P., Weingartner, R., and Hegg, C.: Investigations on the runoff generation at the profile and plot scales, Swiss Emmental, Hydrol. Process., 20, 377-394, https://doi.org/10.1002/hyp.6056, 2006.

Barron, O. V., Pollock, D., and Dawes, W.: Evaluation of catchment contributing areas and storm runoff in flat terrain subject to urbanisation, Hydrol. Earth Syst. Sci., 15, 547-559, https://doi.org/10.5194/hess-15-547-2011, 2011.

Blöschl, G.: Three hypotheses on changing river flood hazards, Hydrol. Earth Syst. Sci., 26, 5015-5033, https://doi.org/10.5194/hess-26-5015-2022, 2022.

Bracken, L. J., Wainwright, J., Ali, G. A., Tetzlaff, D., Smith, M. W., Reaney, S. M., and Roy, A. G.: Concepts of hydrological connectivity: Research approaches, pathways and future agendas, Earth-Science Reviews, 119, 17-34, https://doi.org/10.1016/j.earscirev.2013.02.001, 2013.

Brêda, J. P. L. F., Melsen, L. A., Athanasiadis, I., Van Dijk, A., Siqueira, V. A., Verhoef, A., Zeng, Y., and van der Ploeg, M.: Predictor Importance for Hydrological Fluxes of Global Hydrological and Land Surface Models, Water Resour. Res., 60, https://doi.org/10.1029/2023wr036418, 2024.

Breiman, L.: Random forests, Machine Learning, 45, 5-32, https://doi.org/10.1023/a:1010933404324, 2001.

Brown, B. C., Fullerton, A. H., Kopp, D., Tromboni, F., Shogren, A. J., Webb, J. A., Ruffing, C., Heaton, M., Kuglerová, L., Allen, D. C., McGill, L., Zarnetske, J. P., Whiles, M. R., Jones, J. B., and Abbott, B. W.: The Music of Rivers: The Mathematics of Waves Reveals Global Structure and Drivers of Streamflow Regime, Water Resour. Res., 59, https://doi.org/10.1029/2023wr034484, 2023.

Bush, S. A., Stallard, R. F., Ebel, B. A., and Barnard, H. R.: Assessing plot-scale impacts of land use on overland flow generation in Central Panama, Hydrol. Process., 34, 5043-5069, https://doi.org/10.1002/hyp.13924, 2020.

Cavalcante, R. B. L., Pontes, P. R. M., Souza, P. W. M., and de Souza, E. B.: Opposite Effects of Climate and Land Use Changes on the Annual Water Balance in the Amazon Arc of Deforestation, Water Resour. Res., 55, 3092-3106, https://doi.org/10.1029/2019wr025083, 2019.

Chen, B., Krajewski, W. F., Helmers, M. J., and Zhang, Z. D.: Spatial Variability and Temporal Persistence of Event Runoff Coefficients for Cropland Hillslopes, Water Resour. Res., 55, 1583-1597, https://doi.org/10.1029/2018wr023576, 2019.

Cheng, S. J., Hulsman, P., Koppa, A., Beck, H. E., Xia, J., Xu, J. J., Cheng, L., and Miralles, D. G.: Global Runoff Partitioning Based on Budyko-Constrained Machine Learning, Water Resour. Res., 61, https://doi.org/10.1029/2025wr039863, 2025.

Costabile, P., Barbero, G., Nagy, E. D., Négyesi, K., Petaccia, G., and Costanzo, C.: Predictive capabilities, robustness and limitations of two event-based approaches for lag time estimation in heterogeneous watersheds, J. Hydrol., 642, https://doi.org/10.1016/j.jhydrol.2024.131814, 2024.

Detty, J. M. and McGuire, K. J.: Threshold changes in storm runoff generation at a till-mantled headwater catchment, Water Resour. Res., 46, https://doi.org/10.1029/2009wr008102, 2010.

Donat, M. G., Lowry, A. L., Alexander, L. V., O'Gorman, P. A., and Maher, N.: More extreme precipitation in the world's dry and wet regions, Nature Climate Change, 6, 508-+, https://doi.org/10.1038/nclimate2941, 2016.

Duan, Q., Sorooshian, S., and Gupta, V.: Effective and efficient global optimization for conceptual rainfall-runoff models. Water Resources Research, 28(4), 1015–1031. https://doi.org/10.1029/91WR02985, 1992.

Färber, C., Plessow, H., Mischel, S., Kratzert, F., Addor, N., Shalev, G., and Looser, U.: GRDC-Caravan: extending Caravan with data from the Global Runoff Data Centre, Earth System Science Data, 17, 4613-4625, https://doi.org/10.5194/essd-17-4613-2025, 2025.

Fidal, J. and Kjeldsen, T. R.: Accounting for soil moisture in rainfall-runoff modelling of urban areas, J. Hydrol., 589, https://doi.org/10.1016/j.jhydrol.2020.125122, 2020.

Giani, G., Rico-Ramirez, M. A., and Woods, R. A.: A Practical, Objective, and Robust Technique to Directly Estimate Catchment Response Time, Water Resour. Res., 57, https://doi.org/10.1029/2020wr028201, 2021.

Gomi, T., Sidle, R. C., Miyata, S., Kosugi, K., and Onda, Y.: Dynamic runoff connectivity of overland flow on steep forested hillslopes: Scale effects and runoff transfer, Water Resour. Res., 44, https://doi.org/10.1029/2007wr005894, 2008a.

Gomi, T., Sidle, R. C., Ueno, M., Miyata, S., and Kosugi, K.: Characteristics of overland flow generation on steep forested hillslopes of central Japan, J. Hydrol., 361, 275-290, https://doi.org/10.1016/j.jhydrol.2008.07.045, 2008b.

Gyasi-Agyei, Y. and Melching, C. S.: Modelling the dependence and internal structure of storm events for continuous rainfall simulation, J. Hydrol., 464, 249-261, https://doi.org/10.1016/j.jhydrol.2012.07.014, 2012.

Han, J., Liu, Z., Woods, R., McVicar, T. R., Yang, D., Wang, T., Hou, Y., Guo, Y., Li, C., and Yang, Y.: Streamflow seasonality in a snow-dwindling world, Nature, 629, 1075-1081, https://doi.org/10.1038/s41586-024-07299-y, 2024.

Harp, R. D. and Horton, D. E.: Observed Changes in Daily Precipitation Intensity in the United States, Geophysical Research Letters, 49, https://doi.org/10.1029/2022gl099955, 2022.

Hashino, M., Yao, H. X., and Yoshida, H.: Studies and evaluations on interception processes during rainfall based on a tank model, J. Hydrol., 255, 1-11, https://doi.org/10.1016/s0022-1694(01)00506-6, 2002.

Herbst, M., Diekkrüger, B., and Vanderborght, J.: Numerical experiments on the sensitivity of runoff generation to the spatial variation of soil hydraulic properties, J. Hydrol., 326, 43-58, https://doi.org/10.1016/j.jhydrol.2005.10.036, 2006.

Hunt, A., Ghanbarian, B., Sahimi, M., and Duan, Q. Y.: Scale Effect on Evapotranspiration: Predicting the Continental and Global Scale Water Balance Based on Percolation Theory and Optimality Principle, Water Resour. Res., 61, https://doi.org/10.1029/2024wr039658, 2025.

Ijjaszvasquez, E. J., Bras, R. L., and Moglen, G. E.: Sensitivity of a basin evolution model to the nature of runoff production and to initial conditions, Water Resour. Res., 28, 2733-2741, https://doi.org/10.1029/92wr01561, 1992.

Iturbide, M., Gutiérrez, J. M., Alves, L. M., Bedia, J., Cerezo-Mota, R., Cimadevilla, E., Cofiño, A. S., Di Luca, A., Faria, S. H., Gorodetskaya, I. V., Hauser, M., Herrera, S., Hennessy, K., Hewitt, H. T., Jones, R. G., Krakovska, S., Manzanas, R., Martínez-Castro, D., Narisma, G. T., Nurhati, I. S., Pinto, I., Seneviratne, S. I., van den Hurk, B., and Vera, C. S.: An update of IPCC climate reference regions for subcontinental analysis of climate model data: definition and aggregated datasets, Earth System Science Data, 12, 2959-2970, https://doi.org/10.5194/essd-12-2959-2020, 2020.

Jehn, F. U., Bestian, K., Breuer, L., Kraft, P., and Houska, T.: Using hydrological and climatic catchment clusters to explore drivers of catchment behavior, Hydrol. Earth Syst. Sci., 24, 1081-1100, https://doi.org/10.5194/hess-24-1081-2020, 2020.

Jiang, S. J., Tarasova, L., Yu, G., and Zscheischler, J.: Compounding effects in flood drivers challenge estimates of extreme river floods, Science Advances, 10, https://doi.org/10.1126/sciadv.adl4005, 2024.

Jiang, Y. J., Zhang, Y. L., Fan, B. H., Wen, J. H., Liu, H., Mello, C. R., Cui, J. F., Yuan, C., and Guo, L.: Preferential flow influences the temporal stability of soil moisture in a headwater catchment, Geoderma, 437, https://doi.org/10.1016/j.geoderma.2023.116590, 2023.

Kang, S. Y., Yin, J. B., Gu, L., Yang, Y. H., Liu, D. D., and Slater, L.: Observation-Constrained Projection of Flood Risks and Socioeconomic Exposure in China, Earths Future, 11, https://doi.org/10.1029/2022ef003308, 2023.

Kemter, M., Marwan, N., Villarini, G., and Merz, B.: Controls on Flood Trends Across the United States, Water Resour. Res., 59, https://doi.org/10.1029/2021wr031673, 2023.

Kinnell, P. I. A.: Applying the RUSLE and the USLE-M on hillslopes where runoff production during an erosion event is spatially variable, J. Hydrol., 519, 3328-3337, https://doi.org/10.1016/j.jhydrol.2014.10.016, 2014.

Kratzert, F., Nearing, G., Addor, N., Erickson, T., Gauch, M., Gilon, O., Gudmundsson, L., Hassidim, A., Klotz, D., Nevo, S., Shalev, G., and Matias, Y.: Caravan - A global community dataset for large-sample hydrology, Sci Data, 10, 61, https://doi.org/10.1038/s41597-023-01975-w, 2023.

Kuhn, N. J. and Yair, A.: Spatial distribution of surface conditions and runoff generation in small arid watersheds, Zin Valley Badlands, Israel, Geomorphology, 57, 183-200, https://doi.org/10.1016/s0169-555x(03)00102-8, 2004.

Li, H. Y. and Sivapalan, M.: Effect of spatial heterogeneity of runoff generation mechanisms on the scaling behavior of event runoff responses in a natural river basin, Water Resour. Res., 47, https://doi.org/10.1029/2010wr009712, 2011.

Li, Y., Zhou, Q. W., Zhao, Y. L., Cai, L. L., Li, K. P., Chen, Z. S., and Guo, Q.: Regulation of shallow soil hydrological processes by rainfall characteristics and vegetation type on karst hillslopes: Insights from plot-scale field experiments, J. Hydrol., 663, https://doi.org/10.1016/j.jhydrol.2025.134199, 2025.

Liang, H., Liu, D., Wang, W., Yue, F., and Zhang, J.: Understanding Multiscale Hydrological Interactions From Spectral Perspective: A Large Sample Investigation Across the United States, Water Resour. Res., 62, e2025WR041886, https://doi.org/10.1029/2025WR041886, 2026.

Liang, W., Bai, D., Wang, F. Y., Fu, B. J., Yan, J. P., Wang, S., Yang, Y. T., Long, D., and Feng, M. Q.: Quantifying the impacts of climate change and ecological restoration on streamflow changes based on a Budyko hydrological model in China's Loess Plateau, Water Resour. Res., 51, 6500-6519, https://doi.org/10.1002/2014wr016589, 2015.

Liu, Z. Y., Yue, Y., Slater, L., Borthwick, A. G. L., Chai, Y. F., Luan, X. F., Miao, C. Y., and Yang, Z. H.: Constrained Precipitation Extremes Reveal Unequal Future Socioeconomic Exposure, Earths Future, 12, https://doi.org/10.1029/2024ef004825, 2024.

López-Vicente, M., García-Ruiz, R., Guzmán, G., Vicente-Vicente, J. L., Van Wesemael, B., and Gómez, J. A.: Temporal stability and patterns of runoff and runon with different cover crops in an olive orchard (SW Andalusia, Spain), Catena, 147, 125-137, https://doi.org/10.1016/j.catena.2016.07.002, 2016.

Lyne, V. and Hollick, M.: Stochastic time-variable rainfall-runoff modelling. In Institute of Engineers Australia National Conference (ed. Ratcliffe, J. S.) 89–93 (Barton, Australia: Institute of Engineers, 1979), 1979.

Mahmood, T. H. and Vivoni, E. R.: A climate-induced threshold in hydrologic response in a semiarid ponderosa pine hillslope, Water Resour. Res., 47, https://doi.org/10.1029/2011wr010384, 2011.

Massari, C., Pellet, V., Tramblay, Y., Crow, W. T., Gründemann, G. J., Hascoet, T., Penna, D., Modanesi, S., Brocca, L., Camici, S., and Marra, F.: On the relation between antecedent basin conditions and runoff coefficient for European floods, J. Hydrol., 625, https://doi.org/10.1016/j.jhydrol.2023.130012, 2023.

Mei, Y. W., Wang, D. G., Zhu, J. X., Tang, G. P., Cai, C. K., Shen, X. Y., Hong, Y., and Zhang, X. X.: Optimal Baseflow Separation Through Chemical Mass Balance: Comparing the Usages of Two Tracers, Two Concentration Estimation Methods, and Four Baseflow Filters, Water Resour. Res., 60, https://doi.org/10.1029/2023wr036386, 2024.

Merz, R. and Blöschl, G.: A regional analysis of event runoff coefficients with respect to climate and catchment characteristics in Austria, Water Resour. Res., 45, https://doi.org/10.1029/2008wr007163, 2009.

Merz, R., Blöschl, G., and Parajka, J.: Spatio-temporal variability of event runoff coefficients, J. Hydrol., 331, 591-604, https://doi.org/10.1016/j.jhydrol.2006.06.008, 2006.

Miller, J. D. and Hess, T.: Urbanisation impacts on storm runoff along a rural-urban gradient, J. Hydrol., 552, 474-489, https://doi.org/10.1016/j.jhydrol.2017.06.025, 2017.

Nash, J. E.: The form of the instantaneous unit hydrograph. IAHS Publ. 45 (3), 114–121, 1957.

Norbiato, D., Borga, M., Merz, R., Blöschl, G., and Carton, A.: Controls on event runoff coefficients in the eastern Italian Alps, J. Hydrol., 375, 312-325, https://doi.org/10.1016/j.jhydrol.2009.06.044, 2009.

Nyssen, J., Clymans, W., Descheemaeker, K., Poesen, J., Vandecasteele, I., Vanmaercke, M., Zenebe, A., Van Camp, M., Haile, M., Haregeweyn, N., Moeyersons, J., Martens, K., Gebreyohannes, T., Deckers, J., and Walraevens, K.: Impact of soil and water conservation measures on catchment hydrological response-a case in north Ethiopia, Hydrol. Process., 24, 1880-1895, https://doi.org/10.1002/hyp.7628, 2010.

O'Shea, D., Nathan, R., Wasko, C., and Hill, P.: Implications of event-based loss model structure on simulating large floods, J. Hydrol., 595, https://doi.org/10.1016/j.jhydrol.2021.126008, 2021.

Oda, T., Iwasaki, K., Egusa, T., Kubota, T., Iwagami, S., Iida, S., Momiyama, H., and Shimizu, T.: Scale-Dependent Inter-Catchment Groundwater Flow in Forested Catchments: Analysis of Multi-Catchment Water Balance Observations in Japan, Water Resour. Res., 60, https://doi.org/10.1029/2024wr037161, 2024.

Ohmura, A. and Wild, M.: Is the hydrological cycle accelerating?, Science, 298, 1345-1346, https://doi.org/10.1126/science.1078972, 2002.

Oki, T. and Kanae, S.: Global hydrological cycles and world water resources, Science, 313, 1068-1072, https://doi.org/10.1126/science.1128845, 2006.

Ombadi, M., Risser, M. D., Rhoades, A. M., and Varadharajan, C.: A warming-induced reduction in snow fraction amplifies rainfall extremes, Nature, 619, 305-+, https://doi.org/10.1038/s41586-023-06092-7, 2023.

Parasuraman, K. and Elshorbagy, A.: Toward improving the reliability of hydrologic prediction: Model structure uncertainty and its quantification using ensemble-based genetic programming framework, Water Resour. Res., 44, https://doi.org/10.1029/2007wr006451, 2008.

Penna, D., Tromp-van Meerveld, H. J., Gobbi, A., Borga, M., and Dalla Fontana, G.: The influence of soil moisture on threshold runoff generation processes in an alpine headwater catchment, Hydrol. Earth Syst. Sci., 15, 689-702, https://doi.org/10.5194/hess-15-689-2011, 2011.

Sadeghi, S. H., Kheirfam, H., and Darki, B. Z.: Controlling runoff generation and soil loss from field experimental plots through inoculating cyanobacteria, J. Hydrol., 585, https://doi.org/10.1016/j.jhydrol.2020.124814, 2020.

Schwemmle, R. and Weiler, M.: Consistent Modeling of Transport Processes and Travel Times-Coupling Soil Hydrologic Processes With StorAge Selection Functions, Water Resour. Res., 60, https://doi.org/10.1029/2023wr034441, 2024.

Sheldon, S. A. and Fiedler, F. R.: Direct numerical simulation of Hortonian runoff resulting from heterogeneous saturated hydraulic conductivity, J. Hydrol. Eng., 13, 948-959, https://doi.org/10.1061/(asce)1084-0699(2008)13:10(948), 2008.

Shelef, E., Griffore, M., Mark, S., Coleman, T., Wondolowski, N., Lasher, G. E., and Abbott, M.: Sensitivity of Erosion-Rate in Permafrost Landscapes to Changing Climatic and Environmental Conditions Based on Lake Sediments From Northwestern Alaska, Earths Future, 10, https://doi.org/10.1029/2022ef002779, 2022.

Sherman, L. K.: Streamflowfromrainfall by unithydrographmethod, Eng. News Records, 108, 501–505, 1932.

Solanki, H., Vegad, U., Kushwaha, A., and Mishra, V.: Improving Streamflow Prediction Using Multiple Hydrological Models and Machine Learning Methods, Water Resour. Res., 61, https://doi.org/10.1029/2024wr038192, 2025.

Song, Y. H., Chung, E. S., and Shahid, S.: Global Future Climate Signal by Latitudes Using CMIP6 GCMs, Earths Future, 12, https://doi.org/10.1029/2022ef003183, 2024.

Stein, L., Clark, M. P., Knoben, W. J. M., Pianosi, F., and Woods, R. A.: How Do Climate and Catchment Attributes Influence Flood Generating Processes? A Large-Sample Study for 671 Catchments Across the Contiguous USA, Water Resour. Res., 57, https://doi.org/10.1029/2020wr028300, 2021.

Sumner, H. R., Wauchope, R. D., Truman, C. C., Dowler, C. C., and Hook, J. E.: Rainfall simulator and plot design for mesoplot runoff studies, Transactions of the Asae, 39, 125-130, 1996.

Tarasova, L., Basso, S., Poncelet, C., and Merz, R.: Exploring Controls on Rainfall-Runoff Events: 2. Regional Patterns and Spatial Controls of Event Characteristics in Germany, Water Resour. Res., 54, 7688-7710, https://doi.org/10.1029/2018wr022588, 2018.

Taye, G., Poesen, J., Van Wesemael, B., Vanmaercke, M., Teka, D., Deckers, J., Goosse, T., Maetens, W., Nyssen, J., Hallet, V., and Haregeweyn, N.: Effects of land use, slope gradient, and soil and water conservation structures on runoff and soil loss in semi-arid Northern Ethiopia, Physical Geography, 34, 236-259, https://doi.org/10.1080/02723646.2013.832098, 2013.

Viglione, A., Merz, R., and Blöschl, G.: On the role of the runoff coefficient in the mapping of rainfall to flood return periods, Hydrol. Earth Syst. Sci., 13, 577-593, https://doi.org/10.5194/hess-13-577-2009, 2009.

Wang, H., Liu, J. G., Klaar, M., Chen, A. F., Gudmundsson, L., and Holden, J.: Anthropogenic climate change has influenced global river flow seasonality, Science, 383, 1009-1014, https://doi.org/10.1126/science.adi9501, 2024.

Wasko, C. and Guo, D. L.: Understanding event runoff coefficient variability across Australia using the hydroEvents R package, Hydrol. Process., 36, https://doi.org/10.1002/hyp.14563, 2022.

Willgoose, G. and Perera, H.: A simple model of saturation excess runoff generation based on geomorphology, steady state soil moisture, Water Resour. Res., 37, 147-155, https://doi.org/10.1029/2000wr900265, 2001.

Wu, S., Zhao, J., Wang, H., and Sivapalan, M.: Regional Patterns and Physical Controls of Streamflow Generation Across the Conterminous United States, Water Resour. Res., 57, e2020WR028086, https://doi.org/https://doi.org/10.1029/2020WR028086, 2021.

Xiao, L. L., Li, R., Cai, F. Y., Wu, P. P., and Pan, L. H.: Effects of vegetation cover and rock embedding landscape types and configurations on regulating runoff generation and sediment yields in karst slope under simulated experiment, J. Hydrol., 661, https://doi.org/10.1016/j.jhydrol.2025.133681, 2025.

Xie, J. X., Liu, X. M., Jasechko, S., Berghuijs, W. R., Wang, K. W., Liu, C. M., Reichstein, M., Jung, M., and Koirala, S.: Majority of global river flow sustained by groundwater, Nature Geoscience, 17, https://doi.org/10.1038/s41561-024-01483-5, 2024.

Yan, H. X., Duan, Z. R., Wigmosta, M. S., Sun, N., Leung, L. R., Thurber, T. B., Gutmann, E. D., and Arnold, J. R.: How Flood Hazards in a Warming Climate Could Be Amplified by Changes in Spatiotemporal Patterns and Mechanisms of Water Available for Runoff, Earths Future, 13, https://doi.org/10.1029/2024ef005619, 2025.

Yang, D. W., Yang, Y. T., and Xia, J.: Hydrological cycle and water resources in a changing world: A review, Geography and Sustainability, 2, 115-122, https://doi.org/10.1016/j.geosus.2021.05.003, 2021.

Yao, L., Leng, G. Y., Yu, L. F., Li, H. Y., Tang, Q. H., Python, A., Hall, J. W., Liao, X. Y., Li, J., Qiu, J. L., Quaas, J., Huang, S. Z., Jin, Y., Zscheischler, J., and Peng, J.: Emergent constraints on global soil moisture projections under climate change, Communications Earth & Environment, 6, https://doi.org/10.1038/s43247-025-02024-7, 2025.

Yin, J. B., Gentine, P., Zhou, S., Sullivan, S. C., Wang, R., Zhang, Y., and Guo, S. L.: Large increase in global storm runoff extremes driven by climate and anthropogenic changes, Nature Communications, 9, https://doi.org/10.1038/s41467-018-06765-2, 2018.

https://doi.org/10.5194/egusphere-2026-1006
Preprint. Discussion started: 4 March 2026

Yin, J. B., Guo, S. L., Gentine, P., Sullivan, S. C., Gu, L., He, S. K., Chen, J., and Liu, P.: Does the Hook Structure Constrain Future Flood Intensification Under Anthropogenic Climate Warming?, Water Resour. Res., 57, https://doi.org/10.1029/2020wr028491, 2021.

Zhan, S., Song, C. Q., Wang, J. D., Sheng, Y. W., and Quan, J. P.: A Global Assessment of Terrestrial Evapotranspiration Increase Due to Surface Water Area Change, Earths Future, 7, 266-282, https://doi.org/10.1029/2018ef001066, 2019.

Zhang, G. T., Cui, P., Gualtieri, C., Zhang, J. L., Bazai, N. A., Zhang, Z. T., Wang, J., Tang, J. B., Chen, R., and Lei, M. Y.: Stormflow generation in a humid forest watershed controlled by antecedent wetness and rainfall amounts, J. Hydrol., 603, https://doi.org/10.1016/j.jhydrol.2021.127107, 2021.

Zhang, S. L., Zhou, L. M., Zhang, L., Yang, Y. T., Wei, Z. W., Zhou, S., Yang, D. W., Yang, X. F., Wu, X. C., Zhang, Y. Q., Li, X. Y., and Dai, Y. J.: Reconciling disagreement on global river flood changes in a warming climate, Nature Climate Change, 12, 1160-+, https://doi.org/10.1038/s41558-022-01539-7, 2022.

Zhang, Y., Huang, W., Zhang, M., Tian, Y., Wang, G., and Zhong, D.: Atmospheric Basins: Identification of Quasi-Independent Spatial Patterns in the Global Atmospheric Hydrological Cycle Via a Complex Network Approach, Journal of Geophysical Research: Atmospheres, 125, https://doi.org/10.1029/2020jd032796, 2020.

Zhang, Y. C., Long, M. S., Chen, K. Y., Xing, L. X., Jin, R. H., Jordan, M. I., and Wang, J. M.: Skilful nowcasting of extreme precipitation with NowcastNet, Nature, 619, 526-+, https://doi.org/10.1038/s41586-023-06184-4, 2023.

Zheng, Y., Coxon, G., Woods, R., Li, J., and Feng, P.: Controls on the Spatial and Temporal Patterns of Rainfall-Runoff Event Characteristics—A Large Sample of Catchments Across Great Britain, Water Resour. Res., 59, https://doi.org/10.1029/2022wr033226, 2023a.

Zheng, Y. C., Coxon, G., Woods, R., Li, J. Z., and Feng, P.: Controls on the Spatial and Temporal Patterns of Rainfall-Runoff Event Characteristics-A Large Sample of Catchments Across Great Britain, Water Resour. Res., 59, https://doi.org/10.1029/2022wr033226, 2023b.

Ziegler, A. D., Giambelluca, T. W., Plondke, D., Leisz, S., Tran, L. T., Fox, J., Nullet, M. A., Vogler, J. B., Troung, D. M., and Vien, T. D.: Hydrological consequences of landscape fragmentation in mountainous northern Vietnam: Buffering of Hortonian overland flow, J. Hydrol., 337, 52-67, https://doi.org/10.1016/j.jhydrol.2007.01.031, 2007.